Crystals **2012**, *2*, 266-283; doi:10.3390/cryst2020266

OPEN ACCESS

crystals

ISSN 2073-4352

www.mdpi.com/journal/crystals

Review

Theory of Dirac Electrons in Organic Conductors

Yoshikazu Suzumura * and Akito Kobayashi

Department of Physics, Nagoya University, Nagoya 464-8602, Japan;
E-Mail: akito@s.phys.nagoya-u.ac.jp

***** Author to whom correspondence should be addressed; E-Mail: suzumura@s.phys.nagoya-u.ac.jp; Tel.: +81-52-789-2437; Fax: +81-52-789-2928.

Received: 26 March 2012; in revised form: 10 April 2012 / Accepted: 10 April 2012 / Published: 20 April 2012

Abstract: The dynamical property of electrons with the tilted Dirac cone was examined using the tilted Weyl equation. The polarization function exhibits cusps and nonmonotonic structures by varying both the frequency and the momentum. A pair of tilted Dirac cones exhibits a new plasmon for the intermediate magnitude of momentum owing to the combined effects of two tilted cones. Dirac electrons with the zero-gap state (ZGS) in organic conductor α-(BEDT-TTF)$_2$I$_3$ are examined by calculating the Berry curvature, which displays the peak structure for a pair of Dirac particles between the conduction band and the valence band. The ZGS is theoretically predicted for α-(BEDT-TTF)$_2$NH$_4$Hg(SCN)$_4$ under uniaxial pressure. Examining the band structure of the stripe charge ordered state of α-(BEDT-TTF)$_2$I$_3$ under pressure, we have found a topological transition from a conventional insulator to a new phase of a pair of Dirac electrons with a finite mass. Further, investigating the zero-energy (N = 0) Landau level under a strong magnetic field, we propose ferromagnetism breaking the $SU(2)$ valley-pseudo-spin symmetry, and the phase fluctuations of the order parameters leading to Kosterlitz-Thouless transition at lower temperatures.

Keywords: zero-gap state; α-(BEDT-TTF)$_2$I$_3$; polarization function; plasma frequency; tilted Dirac cone; Berry curvature; tilted Weyl equation; α-(BEDT-TTF)$_2$ NH$_4$Hg(SCN)$_4$; topological transition; massive Dirac particle; quantum Hall ferromagnet; Kosterlitz-Thouless transition; organic conductor

---

1. Introduction

The organic conductor α-(BEDT-TTF)$_2$I$_3$ (BEDT-TTF=bis(ethylene-dithio)tetrathiafulvalene) [1] exhibits a band structure of two-dimensional semimetal or a narrow gap semiconductor as claimed by Mori *et al.* [2] based on the extended Huckel molecular orbital calculation. Actually, under high pressure, the material undergoes the metal-insulator transition [3], and exhibits the peculiar property that the carrier (hole) density and mobility change by about six orders of magnitude [4]. A similar behavior was found under uniaxial pressure [5], but at rather a lower pressure where the crystal structure under uniaxial strain and ambient pressure, and at room and low temperatures has been determined [6]. Using these transfer integrals between molecules [6], massless Dirac fermion has been found [7,8] in the band calculation. This novel state settles the long-standing problem of anomalous transport phenomena under pressure. In such a massless Dirac fermion, a noticeable property is expected due to the tilted Dirac cone. In the tilted Weyl equation [9,10], the magnitude of the tilt is characterized by the parameter $\alpha = v_0/v_c = 0.8$ [11], where $\alpha = 0$ corresponds to the isotropic case. The tilt affects the characteristic temperature dependence of the Hall coefficient [12]. Since the conductor is a layered two-dimensional massless Dirac fermion system [13], the inter-plane magnetoresistance also exhibits noticeable properties, as shown theoretically by the angle dependence of the magnetic field [14]. New phenomena induced by the tilted Dirac cones have been maintained by calculating the transport coefficient under strong magnetic field, *i.e.*, the electric-field-induced lifting of the valley degeneracy [15].

The first discovery of massless Dirac fermion in condensed matter was in graphite [16], where the motions of electrons obey the Weyl equation [17]. Anomalous properties in transport phenomena, e.g., absence of the backward scattering and universal conductivity, have been elucidated theoretically [18] on the bases of this equation, and the experimental evidence was obtained in the context of a single layer in graphite structure, graphene [19]. Compared with graphene, α-(BEDT-TTF)$_2$I$_3$ has three unique features: (1) The layered structure with a highly two-dimensional electronic system, which enables us to use powerful experimental methods for bulk material such as NMR [20,21]; (2) the inner degree of freedom which comes from four BEDT-TTF molecule sites participating in the Dirac fermion in a unit cell; (3) the tilt of the Dirac cone, which produces various new electronic properties as described in the present paper.

This paper reviews recent theoretical studies related to the tiled Dirac cone in organic conductors. The outline is as follows. In section 2, dynamical properties such as electron-hole excitation and collective excitation are examined to verify the role of tilting. Although the electronic state has been studied extensively, the dynamical properties associated with the polarization function are not yet clear compared with those in the isotropic case [22]. The dynamical polarization function with the arbitrary wave vector and frequency is calculated analytically by treating a case where the contact point of the Dirac cone is located below the Fermi energy [23]. A noticeable effect of tilted cone is found in the case of two valleys where a new plasmon appears due to the combined effect of the right cone and the left cone [24]. In section 3, Dirac electrons with the zero-gap state (ZGS) in the organic conductor α-(BEDT-TTF)$_2$I$_3$ are examined by calculating the Berry curvature. In addition to the peak structure for a pair of Dirac particles between the conduction band and the valence band, the other neighboring bands show another pair of peaks of Dirac electrons with a tendency toward merging [25]. In section 4,

the ZGS is theoretically predicted for α-(BEDT-TTF)$_2$ $NH_4Hg(SCN)_4$ under uniaxial pressure [26]. The peaks of the Berry curvature are highly anisotropic at the ambient pressure, while those become nearly isotropic at high pressure. In section 5, we re-examine the band structure of the stripe charge ordered state of α-(BEDT-TTF)$_2$I$_3$ under pressure using an extended Hubbard model [27]. By increasing pressure, we find a topological transition from a conventional insulator with a single-minimum in the dispersion relation to a new phase with a double-minimum. This transition is characterized by the emergence of a pair of Dirac electrons with a finite mass. In section 6, the possible quantum Hall ferromagnet and Kosterlitz-Thouless transition are investigated for the zero-energy (N = 0) Landau level in α-(BEDT-TTF)$_2$I$_3$ under strong magnetic field [28]. Ferromagnetism breaking the $SU(2)$ valley-pseudo-spin symmetry in the N = 0 Landau level is proposed by noting the fact that the scattering processes between valleys becomes non-zero in the case of the tilted Dirac cones. In this case, the phase fluctuations of the order parameters can be described by the XY model leading to a Kosterlitz-Thouless transition at lower temperatures. A summary is given in section 7.

2. Dynamical Polarization Function

We examine the following 2x2 effective Hamiltonian [9] which gives the tilted Weyl equation on the Luttinger-Korn basis at the Dirac point,

$$H^{R(L)} = \sum_{\gamma\gamma'} (H^{R(L)}(k))_{\gamma\gamma'} a_{\gamma k}^{R(L)\dagger} a_{\gamma k}^{R(L)} \tag{1}$$

where the matrix is given by

$$H^{R(L)} = \begin{pmatrix} +(-)v_0 & +(-)v_1 - iv_2 \\ +(-)v_1 + iv_2 & +(-)v_0 \end{pmatrix} \tag{2}$$

Here we define $\xi_{sk}^{R(L)} = +(-)v_0 k_x + s v_c |k|$, (s = +,-) and $\alpha = v_0/v_c$. From the two contact points corresponding to two valleys of cones, we focus on one, which is given by the state located close to $\mathbf{k}_0$. The polarization function per valley is calculated as

$$\prod(\omega) = \sum_{ss'} \left(\frac{-2}{L^2}\right) \sum_{k} |F_s^+(\boldsymbol{k}) F_{s'}(\boldsymbol{k}+\boldsymbol{q})|^2 \frac{f(\xi_{s,k}) - f(\xi_{s,'k+q})}{\omega + i\eta - (\xi_{s,'k+q} - \xi_{s,k})} \tag{3}$$

where $f(\xi) = 1/(1 + \exp[(\xi - \mu)/T]$ with T being the temperature. In terms of the eigen function, $\mathbf{F}_s(\mathbf{k})$, of the 2 × 2 matrix Hamiltonian, we obtain

$$|\boldsymbol{F}_s^\dagger(\boldsymbol{k}) \boldsymbol{F}_{s'}(\boldsymbol{k}')|^2 = \frac{1}{2}[1 + ss' \cos(\theta_{\boldsymbol{k}} - \theta_{\boldsymbol{k}'})]. \tag{4}$$

The polarization function is calculated on the plane of q and ω for respective regions as shown in Figure 1.

Figure 1. Several regions on the q-ω plane for calculating the polarization function (Equation (3)). From [23]. Reproduced with permission from JPSJ.

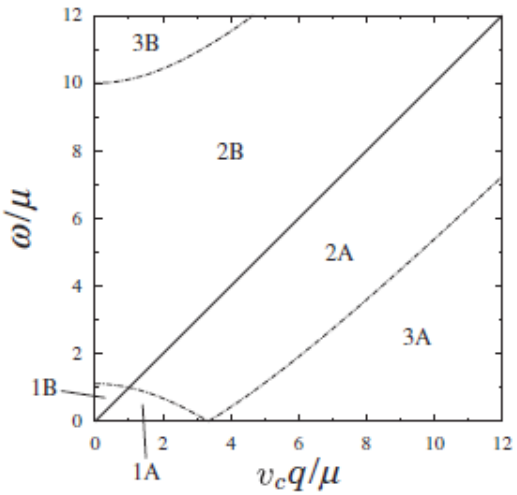

The results consist of six regions. These regions 1A, 2A, 3A, 1B, 2B, and 3B are classified into two regions, A and B, corresponding to the process of intraband and interband excitations, respectively. The regions A and B are separated by a solid line expressed as $\omega_{res} = (1 + \cos\theta_q)v_c q$, which is called the resonance frequency. The resonance frequency is obtained owing to the nesting of the excitations with the linear dispersion, and the polarization function diverges with the chirality factor $\mathbf{F}_s(\mathbf{k})$. The boundary between 2A and 3A is given by ω_+. The boundary between 2A and 1A (2B and 1B) is given by ω_A. The boundary between 2B and 3B is given by ω_B. In the case of the isotropic Dirac cone (*i.e.*, $\alpha = 0$), there is a boundary given by $\omega/\mu + v_c q/\mu = 2$ which separates 1A and 2A (1B and 2B) for the intraband (the interband). In the regions 3A and 1B, the imaginary part vanishes. For the tilted Dirac cone, the boundary between 1A and 2A exhibits a noticeable behavior characterized by the appearance of cusps for the imaginary part as shown in Figure 2.

Figure 2. Normalized imaginary part, Im $\Pi(q,\theta\mathbf{q},\omega)\, v_c^2/\mu$, as a function of ω/μ, for $\theta_q = \pi/2$ and $\alpha = 0.8$. From [23]. Reproduced with permission from JPSJ.

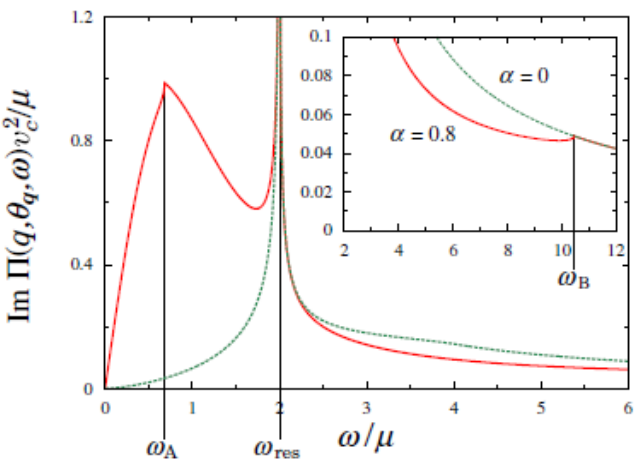

Figure 3 shows the normalized imaginary part, Im $\Pi(\theta\mathbf{q},\omega)\, v_c^2/\mu$, on the plane of $v_c q/\mu$ and ω/μ for $\theta_\mathbf{q} = \pi/2$. The color gauge with the gradation represents the magnitude of the imaginary part. The global

feature is mainly determined by the property of ω_{res}. In the case of $v_c\ q/\mu >> 1$, where the characteristic energy becomes much larger than the interband energy, Im $\Pi(\theta_{\mathbf{q}},\omega)$ of the intraband excitation ($\omega < \omega_{res}$) becomes much smaller than that of the interband excitation ($\omega > \omega_{res}$) in contrast to the case,$v_c\ q/\mu = 2$. The broad peak in the intraband excitation does not change much for $\theta_{\mathbf{q}} < \pi/2$, while it is strongly masked for $\pi/2 < \theta_{\mathbf{q}} < \pi$ due to the rapid decreasing ω_{res}.

Figure 3. Normalized imaginary part, Im $\Pi(\theta\mathbf{q},\omega)\ v_c^2/\mu$, on the plane of $v_c q/\mu$ and ω/μ for $\theta_{\mathbf{q}} = \pi/2$. From [23]. Reproduced with permission from JPSJ.

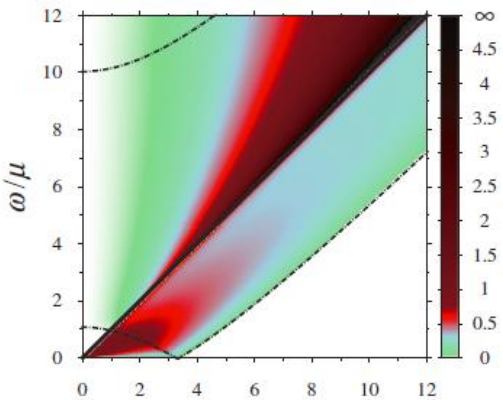

In Figure 4 the normalized optical conductivity of Re$\sigma(\theta_{\mathbf{q}},\omega)$ is shown as a function of ω/μ with some choices of θ $\mathbf{q} = 0$, $\pi/4$ and $\pi/2$, with $\alpha = 0.8$. The dotted line denotes the isotropic case where Re σ is zero for $\omega < \mu$ and is constant for $\mu < \omega$. The conductivity Re σ is zero for $\omega < 2\ \mu/(1 + \alpha)$ and 1 for $\omega > 2\mu/(1 - \alpha)$, while it takes an intermediate value for $2\ \mu/(1 + \alpha) < \omega < 2\mu/(1 - \alpha)$.

Figure 4. Normalized optical conductivity of Re$\sigma(\theta_{\mathbf{q}},\omega)$ as a function of ω/μ. From [23]. Reproduced with permission from JPSJ.

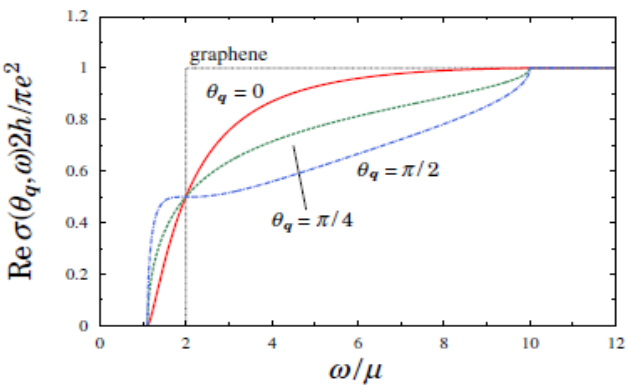

The plasma mode is calculated from $1 + v_q\ \mathrm{Re}\Pi(q,\theta_{\mathbf{q}},\omega_{pl(1,2)}) = 0$ with $v_q = 2\pi e^2/\varepsilon_0 q$. Since the plasma frequency ω_{pl} is located just above the resonance frequency, the solution is expected close to $\omega_{pl1} = \omega^0_{pl1}$ and $\omega_{pl2} = \omega^0_{pl2}$, respectively. However, the imaginary part is complicated due to the combined effects of $\Pi^R(q,\theta_{\mathbf{q}},\omega) + \Pi^L(q,\theta_{\mathbf{q}},\omega)$. We use the scaled quantities as qv_c/μ and ω/μ with $e^2/(\varepsilon_0 v_c) = 1$. The plasma frequency corresponds to ω, which gives a peak of $\mathrm{Im}\Pi_{RPA}(q,\theta_q,\omega)$.

In Figure 5(a), Im $\Pi_{RPA}(q,\theta_q,\omega)$ for $\theta_q = 0$ is shown as a function of $\omega/\mu$with fixed $v_c q/\mu = 0.5$, 0.75, 1, 1.5, 2, 3, 4, 5 and 6, respectively. The dash-dotted line ($\omega_{pl1}(q,\theta\mathbf{q})$ denotes the location of ω/μ for the peak of the plasmon, which is appreciable for small $v_c q/\mu$. The dotted line denotes the location of ω for the novel plasmon, *i.e.*, $\omega_{pl2}(q,\theta\mathbf{q})$, which is found for the intermediate magnitude of $v_c q/\mu$. Such a plasmon, $\omega_{pl2}(q,\theta\mathbf{q})$ originates from the interplay of two tilted cones. These two plasmons, which are found just above ω_{res} are obtained as the hybridization of the electron of the right cone and that of the left cone. The appreciable peak of Im $\Pi_{RPA}(q,\theta_q,\omega)$ moves from $\omega_{pl1}(q,\theta\mathbf{q})$ to $\omega_{pl2}(q,\theta\mathbf{q})$ with increasing q, *i.e.*, the weight for small q is determined by $\omega_{pl1}(q,\theta\mathbf{q})$ and that of intermediate q is determined by $\omega_{pl2}(q,\theta\mathbf{q})$. In Figure 5(b), Im $\Pi_{RPA}(q,\theta_q,\omega)$ is shown for $\theta_q = \pi/4$. It is found that the weight for $\omega_{pl2}(q,\theta\mathbf{q})$ is suppressed. This implies that both the dispersion relation and the intensity exhibit appreciable $\theta\mathbf{q}$ dependence. Such an anisotropy of the intensity gives rise to plasmon filtering. The novel plasmon has the following characteristics. The plasma frequency $\omega_{pl2}(q,\theta\mathbf{q})$ in the case of $\theta\mathbf{q} = 0$ exists for any q. At $\theta_q = \pi/4$, $\omega_{pl2}(q,\theta\mathbf{q})$ does not exist for small q, and is also absent for any q when $\theta_q = \pi/2$. Furthermore, we find that $\omega_{pl1}(q,\theta\mathbf{q})$ is proportional to $q^{1/2}$ for small q, and that $\omega_{pl2}(q,\theta\mathbf{q})$-$\omega_{res}$ is proportional to q for intermediate $v_c q/\mu$.

Figure 5. Im $\Pi_{RPA}(q,\theta_q,\omega)$ as a function of $\omega/\mu$with fixed $v_c q/\mu = 0.5$, 0.75, 1, 1.5, 2, 3, 4, 5 and 6, for $\theta_q = 0$ (**a**), and $\theta_q = \pi/4$ (**b**). From [24]. Reproduced with permission from JPSJ.

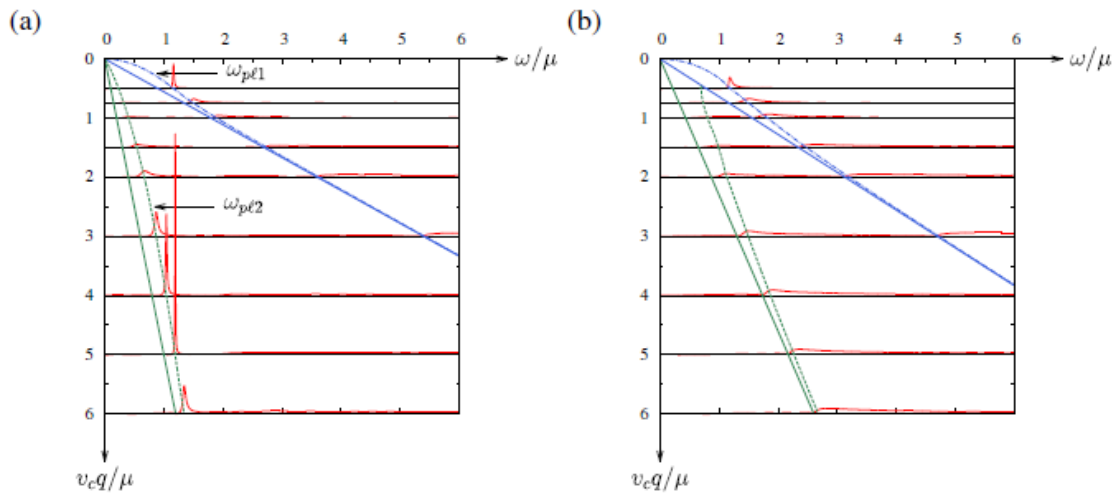

Here we examine the filtering of the plasma frequency by tuning the angle θ_q of the external field with frequency ω and q. Figure 6 is an example of Im $\Pi_{RPA}(q,\theta_q,\omega)$ when the external frequency is chosen as $\omega = \omega_{pl2}(q,0)$ (solid line), $\omega_{pl2}(q,\pi/8)$ (dotted line), and $\omega_{pl2}(q,\pi/4)$ (dashed line) for the fixed $v_c q/\mu = 5$. For $\omega = \omega_{pl2}(q,0)$, a pronounced peak with the peak height (about 15) and the width (0.036 π) shows that the plasmon excitation occurs in the narrow region close to $\theta_q = 0$. For the choice of $\omega = \omega_{pl2}(q,\pi/8)$, the peak appears at $\theta_q = +(-)\pi/8$ where the intensity is reduced less than 1/10 compared with $\omega = \omega_{pl2}(q,0)$. The peak is further reduced for $\omega = \omega_{pl2}(q,\pi/4)$. No peak is expected when the frequency is outside of the regime of the plasma frequency. In terms of the dielectric function $\varepsilon(q,\theta_q,\omega)$, the location of the peak is determined by Re$\varepsilon(q,\theta_q,\omega) = 0$ while the height and the width are determined by Im $\varepsilon(q,\theta_q,\omega)$.Thus the peak (or the double peak) structure gives the filtering of plasmon, which depends on θ_q.

Figure 6. θ_q dependence of Im $\Pi_{RPA}(q,\theta_q,\omega)$ for $v_c q/\mu = 5$ with the fixed $\omega = \omega_{pl2}(q,0)$ (solid line), $\omega_{pl2}(q,\pi/8)$ (dotted line), and $\omega_{pl2}(q,\pi/4)$ (dashed line). From [24]. Reproduced with permission from JPSJ.

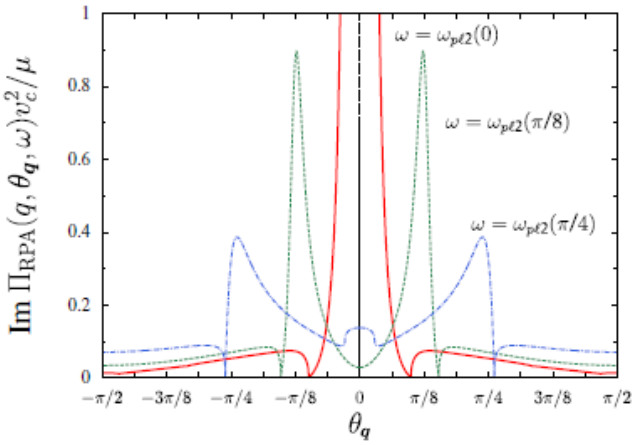

3. Berry Curvature of the Dirac Particle of α-(BEDT-TTF)$_2$I$_3$

The contact point in a normal state, *i.e.*, without charge ordering, is determined essentially by the property of the transfer energy, and the effect of interaction is to modify mainly the location of the contact point. Then, by taking account of only the transfer energy, we examine the Hamiltonian for α-(BEDT-TTF)$_2$I$_3$ given by

$$H=\sum_{\alpha,\beta=1}^{4}\sum_{\sigma}\sum_{i,j}^{N} t_{\alpha,\beta;i,j}\, a^{+}_{\alpha,\sigma,i}\, a_{\beta\sigma,j} \tag{5}$$

where α and β(=1, 2, 3,4) are indices for the site of each molecule A(1), A'(2), B(3) and C(4) in the unit cell, and i, j are those for the cell forming a square lattice with N sites. The quantity *a* denotes the annihilation operator for the electron, and *t* denotes the transfer energy between the neighboring site. As shown in Figure 7, there are seven transfer energies given by t_{b1}, …, t_{b4} for the direction of the b(-x)-axis and t_{a1}, …, t_{a3} for the direction of the a(y) -axis, respectively.

Figure 7. Crystal structure on a two-dimensional plane with four molecules A(1), A'(2), B(3), and C(4), in the unit cell where the respective bonds represent seven transfer energies t_{b1}, ..., t_{a3}. From [25]. Reproduced with permission from JPSJ.

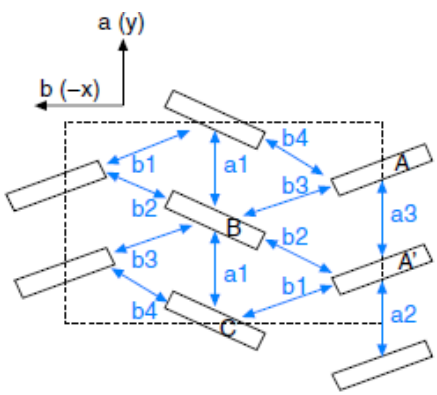

By introducing site potentials given by $I_{1\sigma} = -I_{2\sigma} = -\Delta_0$, and $I_{3\sigma} = -I_{4\sigma} = 0$, the 4×4 Hamiltonian on the site basis and with a Fourier transform is given by

$$H(k)=\begin{pmatrix} -\Delta_0 & t_{c1}+t_{c2}e^{-iky} & t_{p1}-t_{p4}e^{ikx} & t_{p2}-t_{p3}e^{ikx} \\ t_{c1}+t_{c2}e^{iky} & \Delta_0 & t_{p4}e^{iky}-t_{p1}e^{ikx+iky} & t_{p3}-t_{p2}e^{ikx} \\ t_{p1}-t_{p4}e^{-ikx} & t_{p4}e^{iky}-t_{p1}e^{-ikx-iky} & 0 & t_{c3}+t_{c4}e^{-iky} \\ t_{p2}-t_{p3}e^{-ikx} & t_{p3}-t_{p2}e^{-ikx} & t_{c3}+t_{c4}e^{iky} & 0 \end{pmatrix} \quad (6)$$

In the above Hamiltonian, k_x is replaced by $k_x + \pi$ and then the center corresponds to X point. We obtain four bands $E_j(\mathbf{k})$ where $E_1 > E_2 > E_3 > E_4$. For $\Delta_0 = 0$, the inversion symmetry between A and A' is kept, and E_1 and E_2 touches at Dirac point, $\mathbf{k}_0$, where the ZGS is found for the uniaxial pressure P_a being larger than 3 kbar. For the calculation of the Berry curvature, we consider the case of a finite value of Δ_0, which induces a gap at the Dirac point.

The Berry curvature $\mathbf{B}_n(\mathbf{k})$ for each band $E_n(\mathbf{k})$ is calculated as [29]

$$\boldsymbol{B}_n(\boldsymbol{k}) = -\,\mathrm{Im} \sum_{m(\neq n)} \frac{\langle n|\nabla_k H|m\rangle \mathrm{x} \langle m|\nabla_k H|n\rangle}{(E_m - En)^2} \quad (7)$$

where |n > denotes the eigen vector of E_n. Note that $\mathbf{B}_1(\mathbf{k})$ is essentially determined by E_1 and E_2, *i.e.*, the effect of E_3 and E_4 is negligibly small within our numerical calculation. We define $B_n(k)$ as the component of $\mathbf{B}_n(k)$, which is perpendicular to the $k_x - k_y$ plane. For the small limit of Δ_0, we obtain $B_1 = \propto (\Delta_0)^{-2}$.

The energy band and Berry phase under uniaxial P_a are calculated using an extrapolation for t (P_a) [8]. Energy bands of E_1(a) and E_2(b) for Pa =6 kbar and $\Delta_0 = 0.02$ eV is shown in Figure 8(a) and (b).

Figure 8. Energy bands of E_1(a) and E_2(b) for Pa = 6 kbar. From [25]. Reproduced with permission from JPSJ.

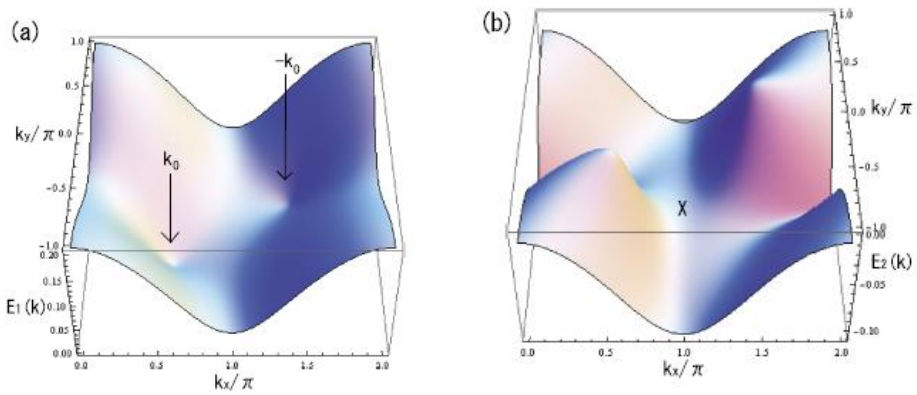

The Dirac cone exists at +(-)$\mathbf{k}_0$, with $\mathbf{k}_0$= (0.57 π, - 0.3 π), as shown by arrows. A pair of cones is seen close to $E_1(\mathbf{k}_0)$ and $E_2(\mathbf{k}_0)$ and the cones in the same band are symmetric with respect to the Γ (=(0,0)) point. For $E_1(\mathbf{k})$, the maximum is seen at the Y(=(0,π)) point, while saddle points are seen for the X(=(0,π)), M(=(π,π)), and Γ points. For $E_2(\mathbf{k})$, the minimum is seen at the M point while saddle

points are seen for the X, Y, and Γ points. The accidental degeneracy, which is found at +(–)$\mathbf{k}_0$ for $-\triangle_0 \rightarrow 0$ is realized as the minimum of $E_1(\mathbf{k})$ and the maximum of $E_2(\mathbf{k})$.

The corresponding Berry curvature $B_1(\mathbf{k})$ is shown in Figure 9. The peak around –$\mathbf{k}_0$ (+$\mathbf{k}_0$) is positive (negative). They are antisymmetric with respect to the Γ. Since the curvature exhibits a noticeable peak close to +(–)$\mathbf{k}_0$, such a peak may be identified as the Dirac particle instead of calculating the contact point.

Figure 9. Berry curvature $B_1(\mathbf{k})$ (component perpendicular to the k_x – k_y plane). From [25]. Reproduced with permission from JPSJ.

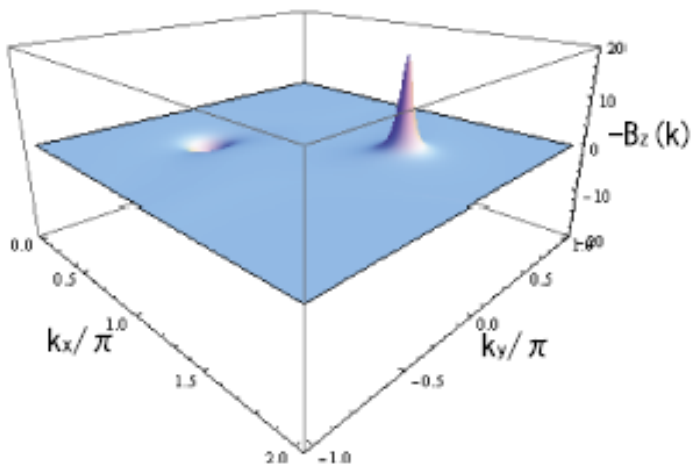

We examined the Berry curvature for other bands. The Berry curvature of the second band $E_2(\mathbf{k})$ is shown for several choices of P_a in Figure 10. The peak located at +(–)$\mathbf{k}_0$ has a sign opposite to that of $E_1(\mathbf{k})$. Figure 10(d) denotes $B_1(\mathbf{k})$ at Pa = 6 kbar corresponding to Figure 9. In addition to such a peak, another pair of peaks appears close to the Γ point. The latter one is rather extended to a direction slightly declined toward the horizontal axis, suggesting a large anisotropy of the Dirac cone. The anisotropic peak disappears for P_a smaller than 3 kbar while it becomes rather isotropic for large P_a. Such a behavior resembles the emergence of the Dirac particle in the charge ordered state, which has been shown in α-(BEDT-TTF)$_2$I$_3$ [27]. The Berry curvature for $E_3(\mathbf{k})$ is obtained similarly where a pair of peaks close to the Γ point also exists with a sign opposite to that of $E_2(\mathbf{k})$. There is another peak close to the M point, which compensates for that of $E_4(\mathbf{k})$. These results show that each neighboring band provides a pair of Dirac particles followed by the Berry curvature with an opposite sign. When a pair of Dirac particles between neighboring two bands is found, one may expect a pair of Dirac particles for the other neighboring bands.

Figure 10. Contour of the Berry curvature, $B_1(\mathbf{k})$, of the second band $E_2(\mathbf{k})$ for Pa = 0(a), 2(b), 4(c), 6(d), 8(e), and 10(f) kbar respectively. Γ = (0,0). The Dirac particle at $\mathbf{k}_0$ with the positive $B_1(\mathbf{k})$ exists in the bright region of $k_x > 0$ and $k_y < 0$.

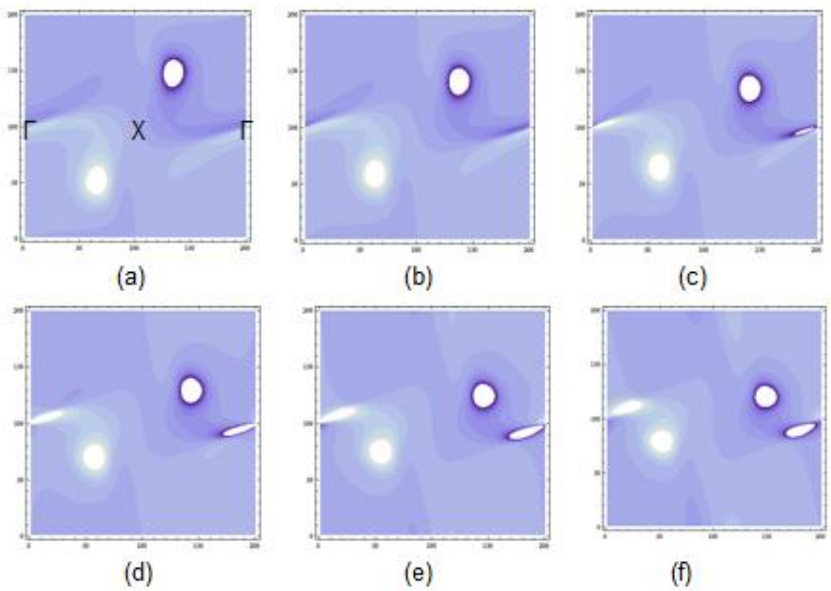

4. Zero-Gap State in α-(BEDT-TTF)$_2$ NH$_4$Hg(SCN)$_4$

In addition to α-(BEDT-TTF)$_2$I$_3$, the ZGS, where a contact point of the Dirac cone coincides with the chemical potential, is predicted for α-(BEDT-TTF)$_2$ NH$_4$Hg(SCN)$_4$ under uniaxial pressure, P_c along the stacking axis [26].

There are the electron and hole surfaces owing to band-overlap at ambient pressure. The ZGS emerges under the uniaxial pressure along the stacking axis in the conducting plane, for $P_c > 5$ kbar. Figure 11 shows the energy dispersions of the conduction and valence band at $P_c = 6$ kbar, where the transfer energies are calculated by extrapolation using the data at $P_c = 0$ kbar [30,31] and 1.5 kbar [31] obtained from the X-ray experiment. A pair of the Dirac cones is located at $k_0 = (-0.25, 0.51)\,\pi$. The chemical potential coincides with the contact points since there is no band-overlap. The Dirac cones are rather isotropic compared with those of α-(BEDT-TTF)$_2$I$_3$.

The singularity of phase of the wave function, which describes the intrinsic property of the Dirac electron, has been confirmed using the Berry curvature. There is a pair of peaks in the Berry curvature, which corresponds to a pair of Dirac electrons with opposite chirality. The peaks of the Berry curvature are highly anisotropic at ambient pressure, while those become nearly isotropic at $P_c = 6$ kbar.

In addition, the effective Hamiltonian on the Luttinger-Kohn representation has been investigated. It has been found that the Dirac cone, which exists below the chemical potential, is anisotropic and tilted at ambient pressure. The anisotropy of the Dirac electron at ambient pressure is related to the one-dimension-like valley (ridge) structure between two contact points in the conduction (valence) band. The anisotropy and tilting of the Dirac cone are reduced with increasing pressure.

Figure 11. Energy dispersions of the conduction and valence band at P_c = 6 kbar of α-(BEDT-TTF)$_2$ $NH_4Hg(SCN)_4$. From [26]. Reproduced with permission from JPSJ.

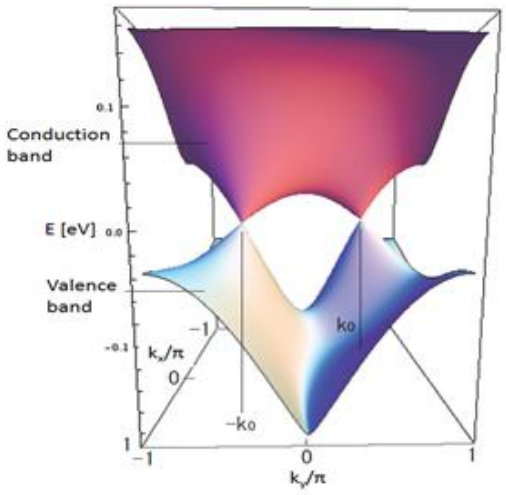

5. Emergence of Dirac Electron Pair in Charge Ordered State of α-(BEDT-TTF)$_2$I$_3$

We re-examined the band structure of the stripe charge ordered state of α-(BEDT-TTF)$_2$I$_3$ under pressure using an extended Hubbard model [27]. The model used to describe the two-dimensional electronic system in α-(BEDT-TTF)$_2$I$_3$ is shown in Figure 12. The unit cell consists of four BEDT-TTF molecules on sites A, A', B and C. The sites A, B and C are inequivalent, while A is equivalent to A' so that inversion symmetry is preserved in the normal state. There are six electrons for the four molecules in a unit cell, *i.e.*, the band is 3/4-filled. On the basis of the HOMO orbitals, the electronic system is described by the extended Hubbard model with several transfer energies, the on-site repulsive interaction U and the anisotropic nearest-neighbor repulsive interaction $V_{\alpha\beta}$,

$$\mathrm{H} = \sum_{(i\alpha,j\beta),\sigma} \left(t_{i\alpha,j\beta} a^{+}_{i\alpha\sigma} a_{j\beta\sigma} + h.c.\right) + \sum_{i\alpha} U a^{+}_{i\alpha\uparrow} a^{+}_{i\alpha\downarrow} a_{i\alpha\downarrow} a_{i\alpha\uparrow} + \sum_{(i\alpha,j\beta),\sigma\sigma'} V_{\alpha\beta} a^{+}_{i\alpha\sigma} a^{+}_{j\beta\sigma'} a_{j\beta\sigma'} a_{i\alpha\sigma} \quad (8)$$

where i, j denote site indices of a given unit cell, and a,b = A, A', B and C are indices of BEDT-TTF sites in the unit cell. In the first term, the transfer energies as a function of a uniaxial pressure (P_a) along the *a*-axis are estimated from an extrapolation using the data at P = 0 kbar [2] and P_a = 2 kbar [6]. We use the parameter U = 0.4 eV and the V_{ab} takes on two different values, V_a = 0.17~0.18 eV along the stacking direction, and V_b = 0.05 eV along the perpendicular direction. With this choice of parameters, we obtain a pressure dependence of the electronic spectrum consistent with experimental results [5]. Throughout the paper, the lattice constant is taken as unity. As in previous work [32], we restrict ourselves to a Hartree mean field theory.

Figure 12. The model describing the electronic system of α-(BEDT-TTF)$_2$I$_3$. The unit cell consists of four BEDT-TTF molecules A, A', B and C with seven transfer energies. The nearest neighbor repulsive interactions are given by Va and Vb [27].

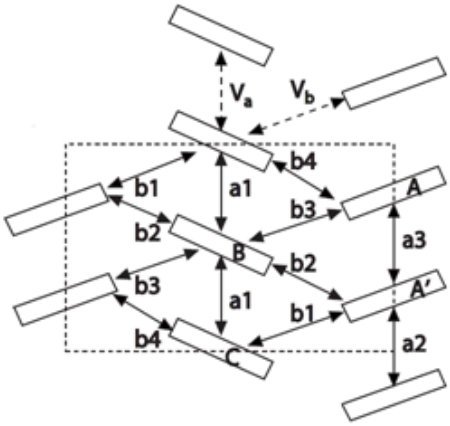

The P_a-V_a phase diagram obtained from the self-consistent Hartree approximation is shown in Figure 13 [27]. This figure exhibits three transition lines. Two of them (the continuous and dashed lines) have already been found in previous work [32] and the third one (dotted line) is a novel transition. The schematic band spectrum close to the Fermi surface is also shown in Figure 13. The solid line marks a charge ordering transition resulting from the simultaneous breaking of time reversal and inversion symmetries. It separates the charge ordered metallic state (COM) from the Zero Gap state (ZGS). In the ZGS phase, energy bands are spin degenerate and inversion symmetry is preserved. Coming from this high-pressure ZGS phase and traversing the continuous line, the inversion symmetry is spontaneously broken by the electronic interactions. As a consequence, a gap opens leading to an insulating phase. However the time reversal symmetry is also spontaneously broken by the interactions so that the degeneracy between up and down bands is now lifted. Therefore the *simultaneous* breaking of time reversal and inversion symmetries results in a semi-metallic phase (COM) with band overlap leading to small electrons and hole pockets of opposite spin orientations. In striking contrast with the continuous line, the dashed line marks a metal-insulator transition from a charge ordered metallic (COM) phase to a charge ordered insulator (CO) without breaking of any symmetry.

In traversing this transition line, the dispersion relations stay similar but their relative positions to the Fermi level vary. In this work, by a more detailed analysis of the COM and CO phases, we find a new *topological* transition (dotted line in Figure 13) that further splits each of the COM and CO phases into two phases: COM(I,II) and CO(I,II). This transition concerns a modification in the two energy bands close to the Fermi energy. They correspond to a given value of the spin that we choose to denote as "up". The two other bands (down) are not concerned by this transition. As illustrated in Figure 13, the transition from CO(I) to CO(II) is characterized by a change in the form of the dispersion relation of the valence and conduction bands. In the CO(I) phase, there is a single minimum of charge gap whose position in the k space stays at the M-point. In the CO(II) phase, the single charge gap separates into two points at symmetrical positions from the M-point. There is now a double-well structure in the dispersion relation. This transition corresponds to the emergence of a pair of Dirac points.

Figure 13. The phase diagram on the *Pa*-*Va* plane, where U = 0.4 eV, and Vb = 0.05 eV [27]. The CO and COM denote insulating and metallic states with charge ordering ,respectively. Phase (I) shows a single minimum, while phase (II) is characterized by a double minimum in the up spin band. In the schematic energy spectrum close to the Fermi energy (horizontal line), the red and blue bands correspond to the up and down spin band, respectively.

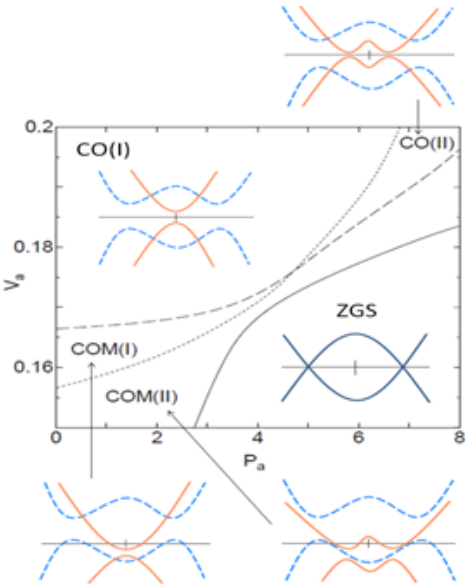

This modification of the band structure is described by an effective low energy Luttinger-Kohn Hamiltonian with nine parameters that can be extracted from a numerical Hartree calculation. From a detailed study of this Hamiltonian and the corresponding energy spectrum, we show that the transition is driven by a single quantity detS_M whose sign changes at the transition. S_M is the stability matrix, which governs the stability of the M-point [27]. A similar scenario occurs for the COM(I)-COM(II) transition.

The existence of a pair of Dirac points is characterized by a special structure of the Berry curvature. In the CO(II) and COM(II) states, the Berry curvature shows two sharp peaks with opposite signs. On the other hand, in CO(I) and COM(I) phases, the Berry curvature becomes very small owing to cancelation of the positive and negative contributions. The existence of the Dirac point is also verified by integrating the Berry curvature over a region limited by a closed energy contour around a single point [27].

This topological transition could be probed in a magnetic field by the modification of the Landau level structure, therefore by *e.g.* magnetoresistance experiments.

6. Tilted-Cone-Induced Easy-Plane Pseudo-Spin Ferromagnet and Kosterlitz-Thouless Transition in Massless Dirac Fermions

We have considered the low-energy effective Hamiltonian for $N = 0$ Landau states in a pair of tilted Dirac cones [28] using the bases of the Wannier functions [33] for the magnetic rectangular lattice, which is constructed by a linear combination of the wave functions of $N = 0$ Landau states in the

Landau gauge. This Wannier functions satisfy orthonormality and are localized around $\boldsymbol{R} = (ma, nb)$ with integers m and n. A unit cell satisfies $ab = 2\pi l^2$ with the magnetic length $l = (hc/2\pi eH)^{1/2}$ and has a magnetic flux quantum hc/e. By taking the long-range Coulomb interaction and the Zeeman energy E_Z, the low-energy effective Hamiltonian is given by

$$H_{eff} = \sum_{i\sigma\tau}(-\sigma E_Z)c^{+}_{i\sigma\tau}c_{i\sigma\tau} + \sum_{ijkl\sigma\sigma'\tau\tau'} V_{ijkl}c^{+}_{i\sigma\tau}c_{j\sigma\tau}c^{+}_{k\sigma'\tau'}c_{l\sigma'\tau'} + \sum_{ijkl\sigma\sigma'\tau} W_{ijkl}c^{+}_{i\sigma,-\tau}c_{j\sigma\tau}c^{+}_{k\sigma'\tau}c_{l\sigma',-\tau} \quad (9)$$

where i, j, k, and l denote the unit cells of the magnetic rectangular lattice at $\boldsymbol{R}_i$, $\boldsymbol{R}_j$, $\boldsymbol{R}_k$, and $\boldsymbol{R}_l$, respectively, σ denote the spin, τ denote the valley-pseudo-spin which represents the degree of freedom on a pair of Dirac cones, and $c_{i\sigma\tau}^{+}$ ($c_{i\sigma\tau}$) is the creation (annihilation) operator on the bases of the Wannier functions. The forward-scattering term of the long-range Coulomb interaction, V_{ijkl}, comes from the long wave length part. This term does not depend on the spin and valley-pseudo-spin, and then it does not break the *SU(4)* symmetry, neither in the spin subspace nor in that of the pseudo-spin. It has been found that the forward-scattering term is not affected by the tilting. On the other hand, the backscattering term of the long-range Coulomb interaction, W_{ijkl}, which is the inter-valley scattering term exchanging large momentum $2\boldsymbol{k}_0$ and breaks the *SU(2)* symmetry in the subspace of the valley-pseudo-spin, comes from the short wave length part. In the absence of tilting, as e.g., in graphene, the backscattering term vanishes. We found that the tilting is essential to have a non-zero backscattering term. The ratio between the forward and backscattering terms is given by $W_{ijkl}/V_{ijkl} \sim \alpha^2 \alpha_L/l$, where α is the tilting parameter, α_L is the real lattice constant. The backscattering term is proportional to α_L, since the large momentum $|2\boldsymbol{k}_0| \sim \pi/\alpha_L$ is exchanged. We note that the lattice constant of α-(BEDT-TTF)$_2$I$_3$, α_L~1 nm, is much larger than that of graphene. Thus it is expected that the backscattering term plays an important role for electron-correlation effects in α-(BEDT-TTF)$_2$I$_3$. The typical value of the ratio W_{ijkl}/V_{ijkl} is approximately 0.07 for α-(BEDT-TTF)$_2$I$_3$ at H = 10 T using the tilting parameter α = 0.8.

In the absence of an explicit symmetry breaking, such as the Zeeman effect or the above-mentioned backscattering term, no particular spin or valley-pseudo-spin channel is selected, and one may even find an entangled spin-pseudo-spin ferromagnetic state at low temperature. The symmetry-breaking terms may, thus, be viewed as ones that choose a particular channel (spin or valley-pseudo-spin) and direction of a pre-existing ferromagnetic state by explicitly breaking the original *SU(4)* symmetry.

In the spin-polarized state without valley-pseudo-spin polarization (Δ = 0), electrons reside in the spin-up branches of the N = 0 Landau levels as shown on the left hand side of Figure 14, where m is the spin polarization and I is the on-site effective interaction in the magnetic rectangular lattice. In the valley-pseudo-spin ferromagnetic state, where the easy-plane (XY) pseudo-spin polarization lifts the valley-pseudo-spin degeneracy and then the spin polarization is suppressed as shown on the right hand side of Figure 14. Although the mean field approximation gives the first order transition from the spin-polarized state to the valley-pseudo-spin-polarized state with decreasing temperature, the valley splitting of Landau levels owing to the partial valley-pseudo-spin polarization may occur continuously with decreasing temperature owing to the two-dimensional fluctuation. Actually, the valley-splitting has been observed in the interlayer magnetoresistance [34].

Figure 14. Schematic figure of the energy levels in the spin-polarized state (left hand side) and the valley-pseudo-spin ferromagnetic state (right hand side). Blue and orange arrows denote the real spins, and μ is the chemical potential. From [28]. Reproduced with permission from JPSJ.

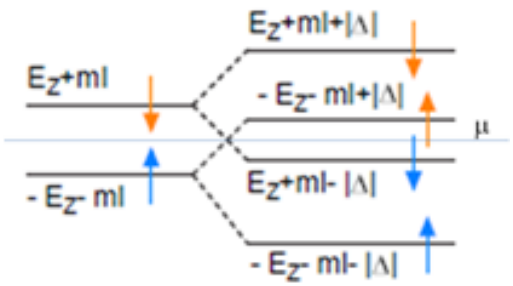

In the presence of the order parameter with a finite amplitude, phase fluctuation exists with the characteristic length of spatial variation much longer than the fictitious lattice spacing. The effect of this phase fluctuation, which has so far been ignored in the mean-field approximation, is treated on the basis of the Wannier functions and the resulting model is similar to the XY model leading to the Kosterlitz-Thouless transition [28].

7. Summary

In the present review, we have shown the effect of tilting of Dirac cone and the characteristic behavior of the Berry curvature in organic conductors.

The tilting effect is examined by calculating the polarization function of the massless Dirac particle for a finite doping. Using the tilted Weyl equation, the dynamical polarization is calculated to find the anisotropic behavior in optical conductivity and plasma frequency. A new plasma mode appears owing to the combined effect of the two tilted cones, leading to the filtering effect.

We examined the Berry curvature to understand the zero-gap state under the uniaxial pressure. The pronounced peak of the Berry curvature around the Dirac point is obtained by adding a small potential acting on the A and A' sites with opposite signs, which breaks the inversion symmetry. Such a method of calculating the Berry curvature is useful to find the Dirac electron in an organic conductor. In addition to α-(BEDT-TTF)$_2$I$_3$, the zero-gap state is theoretically predicted for the organic conductor α-(BEDT-TTF)$_2$ NH$_4$Hg(SCN)$_4$ under uniaxial pressure. The band structure of the stripe charge ordered state of α-(BEDT-TTF)$_2$I$_3$ is re-examined using an extended Hubbard model. We found a topological transition from a conventional insulator towards a new phase, which is characterized by the emergence of a pair of Dirac electrons with a finite mass.

Finally, by examining the zero-energy $N = 0$ Landau level in α-(BEDT-TTF)$_2$I$_3$ under strong magnetic field, we found the tilted-cone-induced XY valley-pseudo-spin ferromagnetic state and Kosterlitz-Thouless transition as an effect of tilting.

Acknowledgement

The authors are thankful to H. Fukuyama, F. Piechon, G. Montambaux, T. Nishine, and T. Choji for their collaborations in the present work. Y.S. is indebted to the Daiko Foundation for financial aid in the present research. This work was financially supported in part by a Grant-in-Aid for Special Coordination Funds for Promoting Science and Technology (SCF) and for Scientific Research on Innovative Areas 20110002, and by Scientific Research (Nos. 19740205, 22540366, and 23540403) from the Ministry of Education, Culture, Sports, Science and Technology in Japan.

References

1. Bender, K.; Henning, I.; Schweitzer, D.; Dietz, K.; Endres, H.; Keller, H.J. Synthesis, Structure and Physical Properties of a Two-Dimensional Organic Metal, Di[bis(ethylenedithiolo)tetrathiofulvalene] triiodide, $(BEDT\text{-}TTF)^{+}_{2}\,I^{-}_{3}$. *Mol. Cryst. Liq. Cryst.* **1984**, *108*, 359–371.
2. Mori, T.; Kobayashi, A.; Sasaki, Y.; Kobayashi, H.; Saito, G.; Inokuchi, H. Band structure of two types of (BEDT-TTF)2I3. *Chem. Lett.* **1984**, 957–960.
3. Kajita, K.; Ojiro, T.; Fujii, H.; Nishio, Y.; Kobayashi, H.; Kobayashi, A.; Kato, R. Magnetotransport Phenomena of α-Type $(BEDT\text{-}TTF)_2I_3$ under High Pressures. *J. Phys. Soc. Jpn.* **1992**, *61*, 23–26.
4. Tajima, N.; Tamura, M.; Nishio, Y.; Kajita, K.; Iye, Y. Transport property of an organic conductor α-$(BEDT\text{-}TTF)_2I_3$ under high pressure - discovery of a novel type of conductors. *J. Phys. Soc. Jpn.* **2000**, *69*, 543–551.
5. Tajima, N.; Tajima, A.E.; Tamura, M.; Nishio, Y.; Kajita, K. Effects of uniaxial strain on transport properties of organic conductor α-$(BEDT\text{-}TTF)_2I_3$ and discovery of superconductivity. *J. Phys. Soc. Jpn.* **2002**, *71*, 1832–1835.
6. Kondo, R.; Kagoshima, S.; Harada, J. Crystal structure analysis under uniaxial strain at low temperature using a unique design of four-axis x-ray diffractometer with a fixed sample. *Rev. Sci. Instrum.* **2005**, *76*, 093902:1–093902:7.
7. Kobayashi, A.; Katayama, S.; Noguchi, K.; Suzumura, Y. Superconductivity in charge ordered organic conductor: α-$(BEDT\text{-}TTF)_2I_3$ salt. *J. Phys. Soc. Jpn*. **2004**, *73*, 3135–3148.
8. Katayama, S.; Kobayashi, A.; Suzumura, Y. Pressure-induced Zero-gap semiconducting state in organic conductor α-$(BEDT\text{-}TTF)_2I_3$. *J. Phys. Soc. Jpn*. **2006**, *75*, 054705:1–054705:6.
9. Kobayashi, A.; Katayama, S.; Suzumura, Y.; Fukuyama, H. Massless fermions in organic conductor. *J. Phys. Soc. Jpn*. **2007**, *76*, 034711:1–034711:6.
10. Goerbig, M.O.; Fuchs, J.-N.; Montambaux, G.; Piéchon, F. Tilted anisotropic Dirac cones in quinoid-type graphene and *α*-$(BEDT\text{-}TTF)_2I_3$. *Phys. Rev. B* **2008**, *78*, 045415:1–045415:10.
11. Tajima, N.; Sugawara, S.; Kato, R.; Nishio, Y.; Kajita, K. Effect of the zero-mode Landau level on interlayer magnetoresistance in multilayer massless Dirac fermion systems. *Phys. Rev. Lett.* **2009**, *102*, 176403:1–176403:4.
12. Kobayashi, A.; Suzumura, Y.; Fukuyama, H. Hall effect and orbital diamagnetism in zerogap state of molecular conductor α-$(BEDT\text{-}TTF)_2I_3$. *J. Phys. Soc. Jpn.* **2008**, *77*, 064718:1–064718:7.

13. Osada, T. Negative interlayer magnetoresistance and zero-mode Landau level in multilayer Dirac electron systems. *J. Phys. Soc. Jpn.* **2008**, *77*, 084711:1–084711:5.
14. Morinari, T.; Himura, T.; Tohyama, T. Possible verification of tilted anisotropic Dirac cone in α-(BEDT-TTF)$_2$I$_3$ using interlayer magnetoresistance. *J. Phys. Soc. Jpn.* **2009**, *78*, 023704:1–023704:4.
15. Goerbig, M.O.; Fuchs, J.-N.; Montambaux, G.; Piéchon, F. Electric-field–induced lifting of the valley degeneracy in α-(BEDT-TTF)$_2$I$_3$ Dirac-like Landau levels. *Eur. Phys. Lett.* **2009**, *85*, 570051:1–570051:5.
16. Wallace, P.R. The band theory of graphite. *Phys. Rev.* **1947**, *71*, 622–634.
17. McClure, J.W. Diamagnetism of graphite. *Phys. Rev.* **1956**, 104, 666–671.
18. Ando, T. Theory of electronic states and transport in carbon nanotubes. *J. Phys. Soc. Jpn.* **2005**, *74*, 777–817.
19. Novoselov, K.S.; Geim, A.K.; Morozov, S.V.; Jiang, D.; Katsnelson, M.I.; Grigorieva, I.V.; Dubonos, S.V.; Firsov, A.A. Two-dimensional gas of massless Dirac fermions in grapheme. *Nature* **2005**, *438*, 197–200.
20. Takano, Y.; Hiraki, K.; Takada, Y.; Yamamoto, H.M.; Takahashi, T. Local spin susceptibility characteristic of zero-gap state of α-(BEDT-TTF)$_2$I$_3$ under pressure. *J. Phys. Soc. Jpn.* **2010**, *79*, 104704:1–104704:7.
21. Miyagawa, K.; Hirayama, M.; Tamura, M.; Kanoda, K. ^{13}C NMR study on zero-gap state in the organic conductor θ-(BEDT-TTF)$_2$I$_3$ under pressure. *J. Phys. Soc. Jpn.* **2010**, *79*, 063703:1–063703:3.
22. Wunsch, B.; Stauber, T.; Sols, F.; Guinea, F. Dynamical polarization of grapheme at finite doping. *N. J. Phys.* **2006**, *8*, 318:1–318:15.
23. Nishine, T.; Kobayashi, A.; Suzumura, Y. Tilted-cone induced cusps and nonmonotonic structures. *J. Phys. Soc. Jpn.* **2010**, *79*, 114715:1–114715:14.
24. Nishine, T.; Kobayashi, A.; Suzumura, Y. New plasmon and filtering effect in a pair of tilted Dirac cone. *J. Phys. Soc. Jpn.* **2011**, *80*, 114713:1–114713:6.
25. Suzumura, Y.; Kobayashi, A. Berry curvature of the Dirac particle in α-(BEDT-TTF)$_2$I$_3$ *J. Phys. Soc. Jpn.* **2011**, *80*, 104701:1–104701:8.
26. Choji, T.; Kobayashi, A.; Suzumura, Y. Zero-gap state in organic conductor α-(BEDT-TTF)$_2$NH$_4$Hg(SCN)$_4$. *J. Phys. Soc. Jpn.* **2011**, *80*, 074712:1–074712:6.
27. Kobayashi, A.; Suzumura, Y.; Piechon, F.; Montambaux, G. Emergence of Dirac electron pair in the charge-ordered state of the organic conductor α-(BEDT-TTF)$_2$I$_3$. *Phys. Rev. B* **2011**, *84*, 075450:1–075450:11.
28. Kobayashi, A.; Suzumura, Y.; Fukuyama, H.; Goerbig, M.O. Tilted-Cone-induced easy-plane pseudo-spin ferromagnet and Kosterlitz-Thouless transition in massless Dirac fermions. *J. Phys. Soc. Jpn.* **2009**, *78*, 114711:1–114711:7.
29. Berry, M.V. Quantal phase factors accompanying adiabatic changes. *Proc. R. Soc. Lond.* **1987**, *A392*, 45–57.
30. Mori, H.; Tanaka, S.; Oshima, M.; Saito, G.; Mori, T.; Maruyama, Y.; Inokuchi, H. Crystal and Electronic Structures of (BEDT–TTF)$_2$[MHg(SCN)$_4$](M=K and NH$_4$). *Bull. Chem. Soc. Jpn.* **1990**, *63*, 2183–2190.

31. Kondo, R.; Kagoshima, S.; Maesato, M. Crystal structure and electronic band structure of the organic superconductor α-(BEDT-TTF)$_2$NH$_4$Hg(SCN)$_4$ under uniaxial strain. *Phys. Rev. B* **2003**, *67*, 134519:1–134519:6.
32. Kobayashi, A.; Katayama, S.; Suzumura, Y. Superconductivity in charge ordered metal for quasi-two-dimensional organic conductor. *J. Phys. Soc. Jpn.* **2005**, *74*, 2897–2900.
33. Fukuyama, H. Tokyo University of Science, Tokyo, Japan. Unpublished work, 1977.
34. Tajima, N.; Sato, M.; Sugawara, S.; Kato, R.; Nishio, Y.; Kajita, K. Spin and valley splittings in multilayered massless Dirac fermion system. *Phys. Rev. B* **2010**, *82*, 121420:1–121424:4.